SCIENCE CHINA
Information Sciences

• RESEARCH PAPER •

August 2026, Vol. 69, Iss. 8, 182401:1–182401:12
https://doi.org/10.1007/s11432-025-4827-y

A high-performance hydrogen sensor for application in distributed gas monitoring networks

Xin LIU[1,2], Huabin YANG[1,2,3], Hanhui LI[1,2], Qiming GUO[1,2], Baile CUI[2,4], Haiyang MAO[1,2,3*] & Na ZHOU[1,2*]

[1]*Institute of Microelectronics of Chinese Academy of Sciences, Beijing 100029, China*
[2]*School of Integrated Circuits, University of Chinese Academy of Sciences, Beijing 101408, China*
[3]*Shandong Key Laboratory of Intelligent Sensing Chips and System, Qingdao 266100, China*
[4]*Institute of Acoustics, Chinese Academy of Sciences, Beijing 100190, China*

Received 10 November 2025/Revised 8 January 2026/Accepted 28 February 2026/Published online 16 July 2026

Abstract With the rapid development of hydrogen energy technology, ensuring the safety and high efficiency of its application necessitates real-time and accurate monitoring of hydrogen concentration, which imposes higher requirements for high-performance hydrogen sensors. However, current hydrogen sensors are often constrained by factors such as size, detection range, sensitivity, and mass production capability, making it difficult to achieve large-scale and distributed monitoring applications within hydrogen energy systems. This study develops a micro-electromechanical systems (MEMS) hydrogen sensor operating on the thermal conductivity sensing principle, utilizing complementary metal oxide semiconductor (CMOS) technology to integrate a heating unit and a thermal sensing unit. By arranging the microheater and a double-layer stacked thermocouple in an equidistant diagonal arrangement and vertical distribution design, and combining it with a back cavity release to form a closed membrane-type structure, the device achieves precise control over temperature and its gradient, as well as efficient thermoelectric conversion. Results show that the device maintains low power consumption and rapid response while achieving a sensitivity of 27.06 mV/%, with a limit of detection (LOD) as low as 20 ppm for hydrogen, demonstrating significant advantages in hydrogen concentration detection. Furthermore, through cross-calculation data from multiple sensors for gas mixture, we successfully resolved the concentration information of H_2 in a gas mixture containing N_2, CO_2, CH_4, and H_2, with an error margin within 5%. This work provides an integrated novel gas monitoring method for smart energy networks, with broad application prospects in distributed hydrogen monitoring networks such as hydrogen fuel vehicles, green hydrogen plants, and power generation systems.

Keywords hydrogen sensor, gas thermal conduction, integrated module, CMOS process, mixed gas detection

Citation Liu X, Yang H B, Li H H, et al. A high-performance hydrogen sensor for application in distributed gas monitoring networks. Sci China Inf Sci, 2026, 69(8): 182401, https://doi.org/10.1007/s11432-025-4827-y

1 Introduction

Hydrogen, as a strategic energy source with high energy density and clean properties, is a key carrier for achieving the "dual carbon" goals and promoting energy transition. Its application value is increasingly prominent in fields such as transportation, energy storage, power generation, and industry [1–5]. However, hydrogen has an extremely low ignition energy (0.017 mJ) and a wide explosion range (4%–75%). Moreover, it is colorless, odorless, and disperses rapidly, which makes it highly dangerous [6]. This renders real-time monitoring of hydrogen leakage a critical aspect of ensuring the safe application of hydrogen energy. For instance, at valve interfaces and pipeline welds in hydrogen storage and transportation systems, even minor leakage can gradually accumulate, creating potential hazards and necessitating reliable monitoring for early warning [7,8]. Additionally, in applications such as electrolysis for hydrogen production and fuel cell operation, slight fluctuations in hydrogen concentration directly impact the system's energy efficiency and product quality. Thus, precise monitoring and dynamic regulation of hydrogen concentration are required to ensure the operational efficiency and stability of production and operation [9,10]. These application scenarios impose stringent requirements on hydrogen sensors, including wide-range, high sensitivity, real-time responsiveness, and miniaturization. This has prompted researchers to conduct in-depth exploration into advanced hydrogen sensing technologies and detection systems.

* Corresponding author (email: maohaiyang@ime.ac.com, zhouna@ime.ac.com)

The current mainstream hydrogen gas sensors utilize various sensing principles, including electrochemical [11], semiconductor [12], optical [13], catalytic combustion [14], and thermal conductivity methods. Among these, thermal conductivity hydrogen sensors exhibit the broadest application potential due to their wide dynamic range (0%–100%), low cost, simple structure, high stability, and suitability for use in inert environments. In recent years, advancements in micro-nano fabrication technology have enabled researchers to enhance the performance of thermal conductivity hydrogen sensors through various optimization approaches [15, 16]. For instance, the 3ω sensor designed by Oh et al. [17] employs a suspended structure and narrow metal strip configuration to reduce the limit of detection (LOD) to 1400 ppm. Zhang et al. [18] utilized a suspended bridge structure, serpentine resistive wires, and thermal isolation structure to minimize solid thermal conduction, thereby improving sensitivity to 10.7×10^{-4} $\%^{-1}$. However, such thermal resistor-based designs face inherent challenges. The resistance temperature coefficient constraints of the thermosensitive material, combined with the unavoidable noise introduced by signal conversion circuits, collectively hinder further improvements in detection limits and sensitivity [19].

To overcome the aforementioned challenges, researchers have also explored attempts based on other thermosensitive principles to achieve higher detection sensitivity and accuracy for subtle thermal changes. Ng et al. [20] developed a thermal conductivity hydrogen sensor based on a ScAlN pyroelectric detector, with an LOD as low as 400 ppm. However, the pyroelectric materials, which also exhibit piezoelectric effects, are susceptible to noise interference and require external heat modulation, thereby limiting further optimization of their detection limits and device size. In contrast, thermopile devices based on the Seebeck effect operate without relying on resistance changes or electrical excitation. They directly convert minute temperature gradients into voltage signals with a high signal-to-noise ratio, reducing noise accumulation in intermediate conversion steps while avoiding self-heating effects, thus providing a pathway to overcome low detection limits and enhance sensitivity [21]. Additionally, the integration of microheaters allows the device to operate without external heat sources, making it more suitable for distributed monitoring scenarios with miniaturization and low power consumption requirements [22]. Despite possessing these advantages, current designs of thermopiles for thermal conductivity gas sensing have notable limitations. Early designs with a dual-end arrangement suffered from uneven heat distribution, while subsequent methods utilizing pulsed voltage for self-heating faced issues of low heating efficiency due to the inherently low thermal conductivity of thermoelectric materials. As a result, these designs have failed to achieve satisfactory gas detection performance [23,24]. The detection range and sensitivity primarily depend on the materials and structural design of the device, including the Seebeck coefficient of the thermoelectric material, the thermal conductivity of the supporting membrane, and the position and number of thermocouple junctions relative to the microheaters [25]. Therefore, the rational selection of device materials and innovative integrated structure design of the thermopile and microheater represent key pathways to optimize the detection limits and sensitivity of thermal conductivity hydrogen sensors [26, 27].

Meanwhile, in practical applications, insufficient specificity remains a bottleneck that hinders the application of thermal conductivity gas sensors in complex scenarios. The principle of thermal conductivity sensors fundamentally relies on the differences in gas thermal conductivities for detection; however, the thermal conductive characteristics of various components in mixed gases can overlap, further obscuring the characteristic signals of the target gas and significantly increasing the risk of misjudgment. Even with excellent sensor performance, reliance solely on a single thermal conductivity signal fails to resolve the fundamental challenge of discriminating between distinct gases with comparable thermal conductivities. Consequently, achieving specific recognition of target gases in mixed gas scenarios remains an urgent and unresolved challenge [28].

To address the aforementioned performance bottlenecks and the challenge of hydrogen identification in complex environments, this work develops a hydrogen thermal conductivity sensor (H-TCS) based on a thermopile structure. The sensor employs a dual-element monolithic integrated design combining a heating unit and a thermosensitive unit. This combination enhances structural flexibility and integration efficiency while achieving in-situ and efficient conversion of temperature difference signals into voltage outputs. The four-terminal symmetrical structure, in conjunction with vertical heat conduction paths and a closed-film configuration, shortens heat transfer distance and reduces heat loss, thereby effectively improving heat transfer efficiency between the heating unit and thermosensitive element. Benefiting from these unique structural designs, the H_2 sensor achieves a high sensitivity of 27.06 mV/%, can respond to H_2 as low as 20 ppm, and exhibits low power consumption (44 mW) as well as rapid response ($\sim$8 s), thus meeting the requirements for miniaturization and mass production. Additionally, to meet the demand for specific recognition, we performed decoupling calculations of composite gas characteristic signals using multiple sensors. This enables the separation and concentration detection of hydrogen signals in a four-component mixture of N_2, CO_2, CH_4, and H_2, thereby expanding the sensor's applicability in complex scenarios. The H-TCS developed in this work has significant application value in hydrogen monitoring networks for hydrogen fuel cells, industrial hydrogen production, storage, and transportation, effectively ensuring safety, enhancing hydrogen utilization efficiency, and

promoting development in related fields.

2 Device design and working principle

The thermal conductivity-based sensor detects gases by quantifying the temperature differences caused by changes in gas thermal conductivity. Due to its inherent physical principles, miniaturized design, and high reliability, it holds unique advantages in distributed hydrogen gas sensing (Figure 1(a)). The specific structure and working principle of the designed thermal conductivity hydrogen sensor are illustrated in Figure 1(b). The core unit of the device consists of a microheater as the heating element and a thermopile as the sensing element. The thermal equilibrium state of the microheater is determined by the rates of heat generation and heat dissipation, where the gas thermal conductivity becomes a crucial factor in regulating the thermal balance of the microheater. The gas thermal conductivity responds systematically to changes in its concentration; as the number of gas molecules per unit volume changes, the frequency of molecular collisions that transfer energy and the mean free path of the molecules also change, leading to significant differences in their macroscopic thermal conduction capabilities (Figure 1(b)-I). The closed membrane structure, formed after release of the back cavity, effectively guides the accumulated heat. This design reduces thermal loss while establishing a stable thermal conduction pathway, with the hot end of the device closely associated with the thermal field of the microheater (Figure 1(b)-II). The temperature at the hot end varies with the gas thermal conductivity, directly affecting the temperature difference conditions of the thermopile, which in turn influences the carrier concentration difference at both ends of the thermopile. Ultimately, the difference in voltage output from the thermopile provides the basis for gas concentration detection (Figure 1(b)-III). The relationship model between gas thermal conductivity and sensor output voltage, along with its theoretical analysis, is presented in Figure A1 and Note 1 in Supporting information. The gas thermal conductivity (λ) primarily regulates the heat transfer efficiency at the gas-solid interface and the rate of thermal conduction between molecules, with higher λ values leading to more pronounced enhancements of both heat transfer processes. According to Wilke's theory, the thermal conductivity of a mixed gas (λ_{mix}) is determined by the thermal conductivities of its components and their molecular interactions. As the mole fraction of high thermal conductivity components increases, λ_{mix} rises, enhancing the heat exchange between the microheater and the gas, resulting in a reduced temperature difference at the thermopile and a decrease in output voltage; conversely, a decrease in the mole fraction of high thermal conductivity components leads to an increase in output voltage, demonstrating a linear response relationship. The core performance of thermal conductivity gas sensors is determined by their sensitivity to the gas thermal conduction process, specifically the response capability of the thermosensitive element to the heat source and the proportion of gas thermal conduction in the heat exchange process. Therefore, the key to constructing high-performance thermal conduction devices lies in the structural design, which must optimize thermal insulation, thermal field uniformity, and gas contact area simultaneously.

The sensor structure consists of 60 pairs of N/P-type polysilicon thermocouples, a microheater surrounding the hot junction, and metal electrical connections, with a chip size of 1300 μm × 1300 μm. The microheater is arranged in an X-shaped configuration perpendicular to the hot end, effectively shortening the solid thermal conduction path and reducing thermal resistance. By combining low thermal conductivity support membrane materials with a suspended membrane structure, the solid thermal conduction losses from the silicon substrate can be effectively minimized. The N-type and P-type polysilicon thermocouple strips are arranged in a four-terminal equidistant arrangement in a double-layer stacked structure to enhance the duty cycle of the sensitive area. Additionally, the thermocouple strips of the thermopile are oriented radially perpendicular to the isotherms, ensuring complete traversal through the high-to-low temperature gradient region, which significantly improves the efficiency of temperature difference utilization, thereby ensuring precise detection of temperature fluctuations caused by subtle changes in gas concentration.

To further analyze the device's operational process, we performed multiphysics coupling simulations to obtain the potential and temperature distribution maps of the sensor (Note 2). Taking an input voltage of 2.5 V as an example, the potential field distribution of the microheater is shown in Figure 1(c). When a voltage is applied to the microheater, Joule heating occurs, and heat is conducted to the surrounding environment, as illustrated in the temperature distribution map of the sensor surface in Figure 1(d). The suspended membrane structure focuses heat in the central region, and the symmetric heating from the microheater creates a square uniform temperature area in the core region of the hot end, exhibiting isotherms in a square annular distribution with a radially decreasing temperature trend. Figure 1(e) presents the potential cloud map of the thermopile structure, showing a regular potential gradient field distributed within the thermopile. Furthermore, the output voltage response at a blackbody radiation temperature of 423.15 K can reach 28.3 mV (Figure A2), indicating the device's excellent thermoelectric response capability.

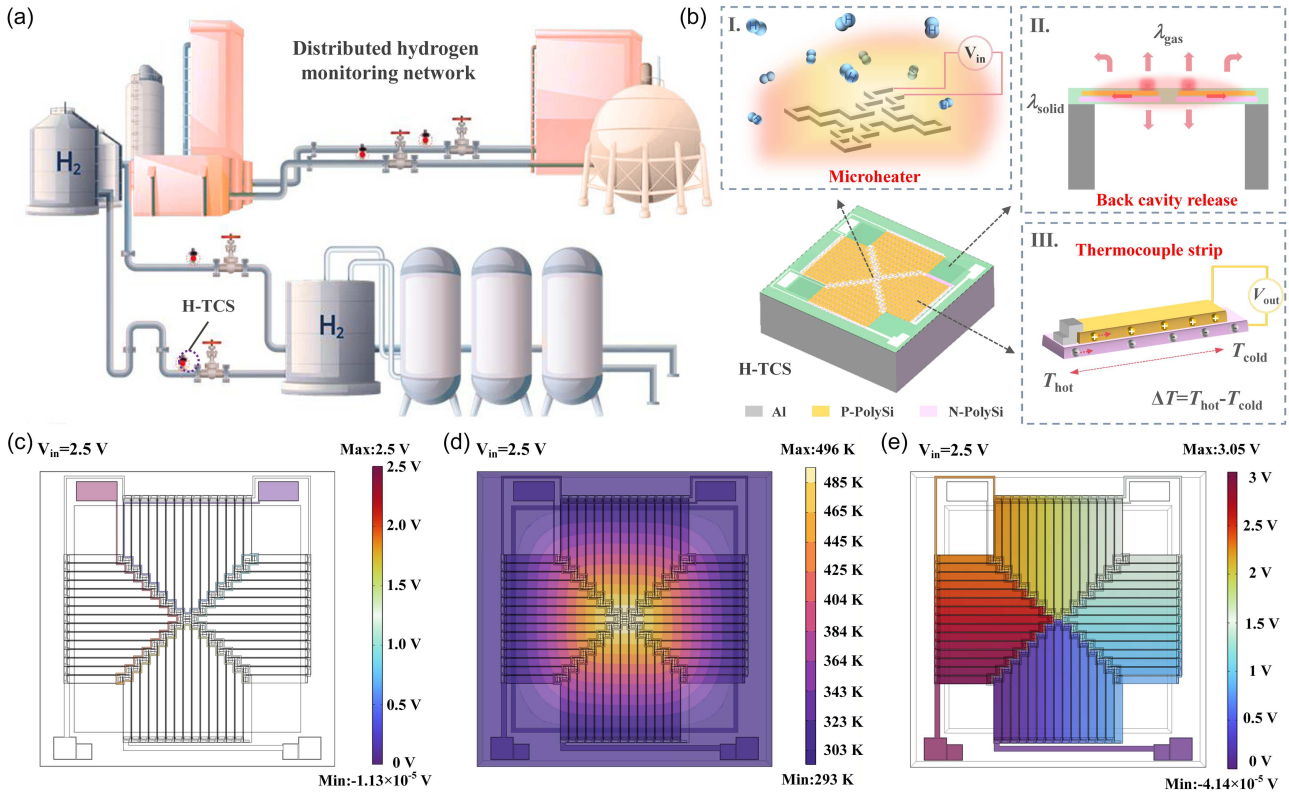

Figure 1 (Color online) Schematic diagram and design of H-TCSs used in a distributed hydrogen monitoring network. (a) Conceptual diagram of H-TCSs applied in distributed hydrogen detection. (b) Schematic drawing of the structure and working principle of the H-TCS, comprising three components: I. a microheater for heating the surrounding gas atmosphere; II. a back cavity release structure optimized for thermal conduction pathways; and III. a thermocouple strip that achieves thermoelectric conversion based on the Seebeck effect. (c) Potential field map of the microheater, (d) isotherm distribution of the H-TCS and (e) potential field map inside the thermocouple stack when the input voltage is 2.5 V.

3 Results and discussion

3.1 Characterization of the H-TCS

Based on the structural design described above, we employed CMOS technology for the wafer-level fabrication of the thermal conductivity hydrogen sensor. The detailed chip fabrication process is illustrated in Figure A3 and Subsection 5.1. A completed 8-inch wafer of the sensor is shown in Figure 2(a). Figure 2(b) presents the surface structure of the chip and high-magnification SEM micrographs of a local area, providing a detailed view of the device's hot and cold end regions as well as the cross-section of the device's membranes. Following fabrication, we encapsulated the device in a TO-39 package to evaluate its performance. The cap was designed with a filter mesh to ensure sufficient contact between the device and the gas molecules while mitigating the impact of gas flow velocity. Additionally, during the encapsulation process, an NTC thermistor was attached, which can be used as a temperature calibration component (Figure A4).

To verify its significant advantages in thermoelectric response performance, we first tested the temperature-voltage response curve of the thermal conductivity sensor under blackbody irradiation, as shown in Figure 2(c). When the blackbody temperature increased from 30°C to 150°C, the output signal rose from 1.38 to 28.94 mV, with the slope of the curve increasing with temperature, indicating a substantial enhancement in device sensitivity as the temperature increased. When an integrated microheater was used as the heating unit, supplying an input voltage ranging from 0.5 to 4.5 V to the microheater caused the center temperature of the sensor to rise continuously, resulting in an increase in output voltage. Simultaneously, we observed that the simulated values of the sensor aligned well with the actual test results, validating the high consistency between the theoretical model and the actual working characteristics (Figures 2(d) and (e)). Detailed infrared thermal imaging can be found in Figure A5. It is noteworthy that the thermal conductivity of the measured gas varies with temperature, as illustrated in Figure A6. The thermal conductivity of the gas exhibits a nearly linear increase within the temperature range of 200–800 K. Consequently, as the surface temperature of the sensor rises, the thermal conductivity of the gas increases, thereby

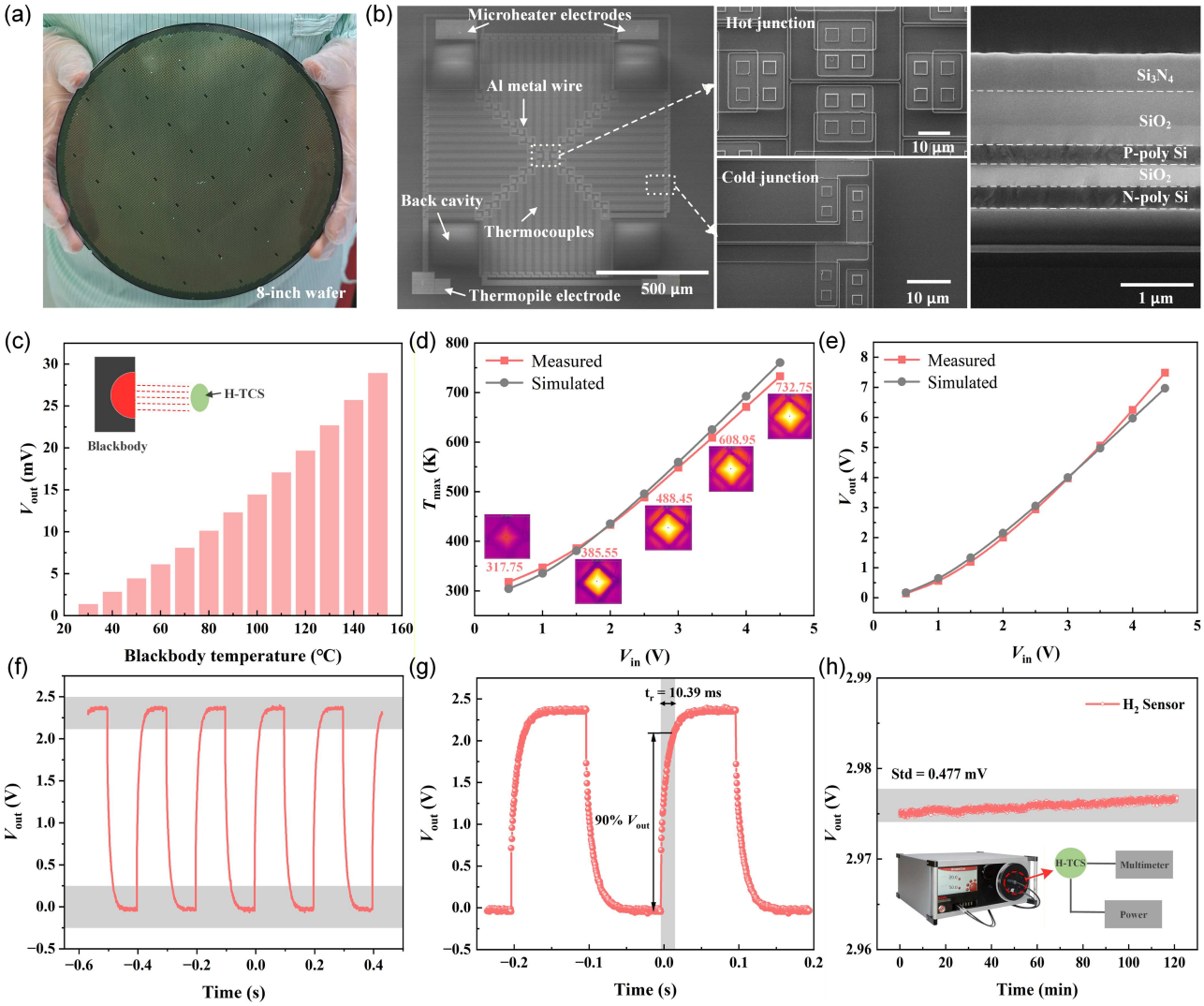

Figure 2 (Color online) Fabrication and thermoelectric performance characterization of H-TCS. (a) Photo of an 8-inch H-TCS wafer. (b) SEM images of the localization of the hot and cold junctions of the thermocouple, along with a cross-section of the sensor, reveal the well-defined film structure of the double-layer stacked polysilicon thermocouple strip. (c) Voltage response curve of the sensor in a temperature range of 30°C to 150°C. Comparison of simulated and experimentally measured data for (d) maximum surface temperature and (e) thermoelectric voltage output of the sensor at varying input voltages. (f) Voltage changes in the sensor during multiple heating cycles. (g) Output waveform of two cycles obtained by the H-TCS, illustrating the thermal response time of the sensor. (h) Long-term voltage variation curve of the sensor.

enhancing the heat transfer efficiency between the micro-heater and the surrounding gas, ultimately modulating the output signal. Moreover, environmental temperature and humidity, as key external variables, can affect the system output. Therefore, we examined the sensor's response within a humidity range of 10% RH to 90% RH (Figure A7(a)). The relatively stable trend in output voltage observed with increasing humidity can be attributed to the similar thermal conductivity of water vapor (~34.7 mW·m^{-1}·K^{-1}/488.45 K) and dry air (~39.1 mW·m^{-1}·K^{-1}/488.45 K). On the other hand, environmental temperature directly influences the temperature difference between the hot and cold ends, with its impact being significantly stronger than that of environmental humidity (Figure A7(b)). High-temperature environments can also exacerbate thermal motion within the thermopile, potentially inducing thermal noise. Therefore, to minimize the interference of environmental parameters on device response, subsequent tests were conducted in a constant temperature and humidity environment. To further assess the stability of the sensor, we tested the voltage response of the H-TCS under a square wave pulse at 2.5 V and 5 Hz. It was observed that the voltage output showed no significant variation over multiple heating cycles (Figure 2(f)). Further analysis revealed the intrinsic response time of the sensor, with the microheater generating heat and transferring it to the hot end of the thermopile, resulting in a stable output with a response time of 10.39 ms (Figure 2(g)). Additionally, the standard deviation of the output voltage variation over two hours of operation was 0.477 mV, indicating good long-term stability (Figure 2(h)).

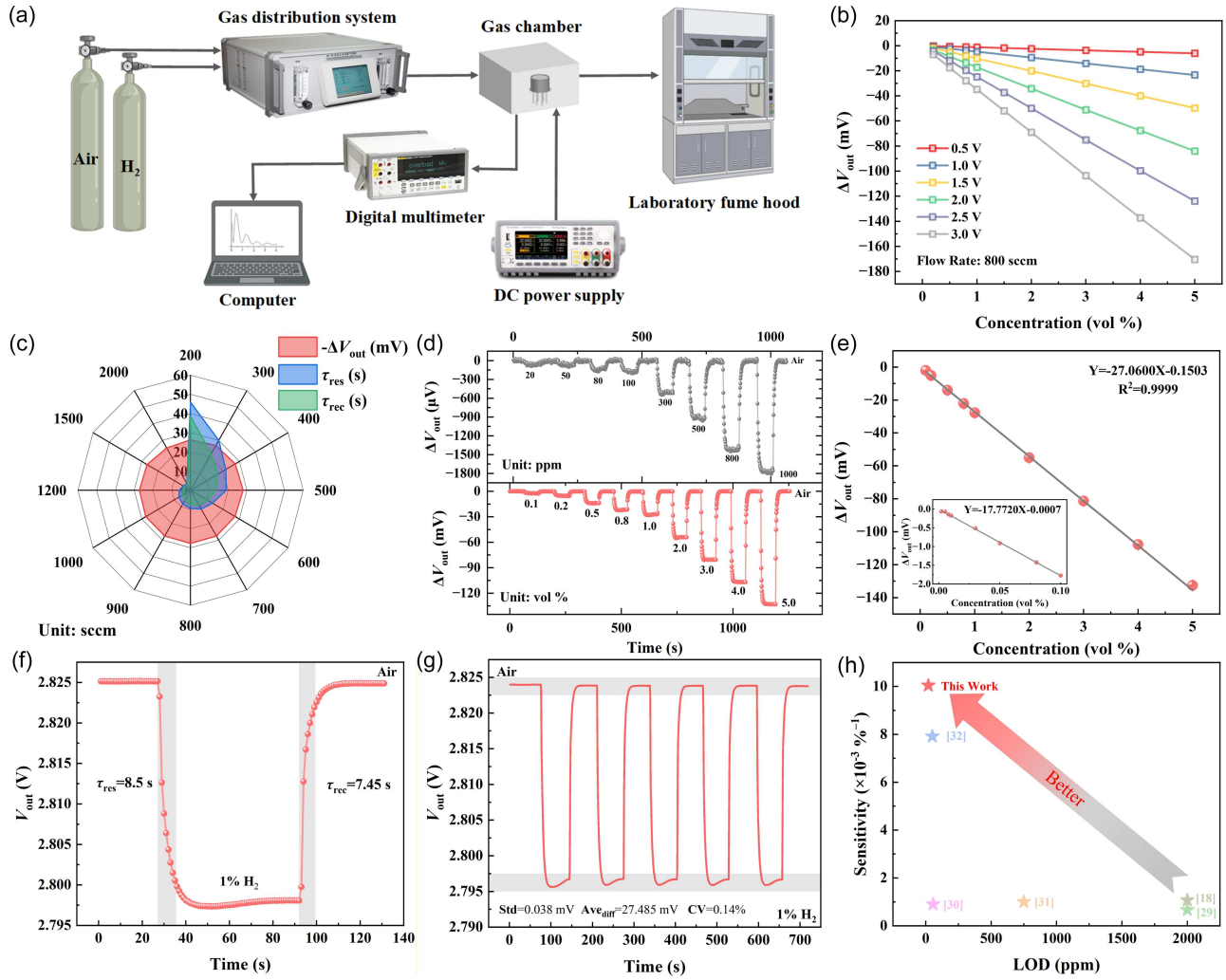

Figure 3 (Color online) Characterization of gas sensing performance of H-TCS. (a) Schematic diagram of the test system for the gas sensor; (b) response curves of output voltage versus hydrogen concentration at different input voltages; (c) radar plots illustrating changes in voltage response, response time and recovery time for varying flow rates of 1% H_2 at 2.5 V; (d) voltage response curves of the sensor at 2.5 V and 800 sccm for H_2 concentrations ranging from 20 ppm to 0.1% and 0.1% to 5.0%, along with (e) the corresponding relationships between gas concentrations and output voltage response; (f) response time and recovery time at a flow rate of 800 sccm @ 1% H_2 concentration; (g) repetitive voltage response curves of the sensor exposed to 1% H_2 over five cycles, where the coefficient of variation (CV) is the ratio of the sample standard deviation to the mean value; (h) performance comparison for hydrogen thermal conductivity sensors [18, 29–32].

3.2 Calibration of the H-TCS

To calibrate the performance of the sensor, we built up a gas testing system consisting of a gas chamber, gas supply unit, gas mixing system, direct current (DC) power supply, digital multimeter, and computer, with specific functions illustrated in Figure 3(a) and described in Subsection 5.2. To find a suitable operating voltage, we compared the output response values of the sensor at different input voltages. Figure 3(b) reveals the voltage response ΔV_{out} (the difference in output voltage when pure dry air and hydrogen are introduced) of the sensor to changes in H_2 concentration under input voltages ranging from 0.5 to 3.0 V. The response sensitivity increases with the rise in input voltage. This is primarily because an increase in input voltage raises the temperature at the hot end. According to Newton's law of cooling, the heat conduction rate $Q \propto \Delta T$, thereby enhancing the efficiency of heat transfer to the gas and improving the thermal exchange with hydrogen, resulting in a significant increase in ΔV_{out} [33]. Additionally, raising the temperature of the microheater can reduce the thermal conductivity difference between the interfering gas and the carrier gas, thus mitigating the impact of interfering gases (such as water vapor) [34]. However, excessively high temperatures may lead to structural deformation of the device, reducing its operational lifespan. Therefore, after weighing the signal strength against device stability, we selected 2.5 V as the operating voltage for the thermal conductivity gas sensor. Under this voltage load, the maximum temperature within the device reached 215.3°C, with a power consumption of 44 mW. Corresponding to this operating temperature, the

thermal conductivity values of all target gases involved in the subsequent analysis were converted based on the data at 488.45 K (i.e., 215.3°C).

Simultaneously, gas thermal conduction is not only related to the thermal conductivity of the gas itself but also influenced by factors such as gas flow rate. Therefore, we used the sensor to detect 1% H_2 at flow rates ranging from 200 to 2000 sccm. The radar plot in Figure 3(c) indicates that the response capability of the developed thermal conductivity hydrogen sensor is largely unaffected by flow rate, while the response and recovery times decrease monotonically with increasing flow rate. This is because an increased flow rate enhances gas replacement efficiency within the chamber, which facilitates a quicker response by reducing the delay and minimizing the retention time of hydrogen during recovery. To balance the need for fast response/recovery time against the noise introduced by airflow turbulence, a flow rate of 800 sccm for H_2 was chosen to obtain fast response and a high signal-to-noise ratio.

The response characteristics and sensitivity to changes in hydrogen concentration are key indicators for assessing the performance of thermal conductivity gas sensors. We characterized these performance parameters by introducing different concentrations of hydrogen at fixed time intervals while simultaneously monitoring the output voltage of the sensor. The dynamic response curves obtained (Figures 3(d) and (e)) show a good linear correlation (R^2= 0.9999) between the sensor's output voltage and hydrogen concentration, with a sensitivity of 27.06 mV/% and a practical detection limit of 20 ppm. Notably, the theoretical detection limit of the sensor is calculated to be 18 ppm (Figure A8 and Note 3), which is slightly lower than the practical detection limit, mainly due to the influence of environmental interference in actual application scenarios. Additionally, we evaluated the device's response performance using 1% H_2 as the detection gas, where the response time and recovery time were 8.5 and 7.45 s, respectively, as shown in Figure 3(f). The response and recovery times of the gas sensor are mainly attributed to the gas replacement rate [35]. In five repeated tests, the ΔV_{out} of the sensor remained essentially unchanged, with a coefficient of variation of 0.14%, indicating excellent repeatability of the device (Figure 3(g)). The selectivity tests in Figure A9 demonstrate that the response amplitude is correlated with the difference in thermal conductivity between the target gas and the carrier gas, with the voltage increase or decrease determined by the relative thermal conductivities of the target gas and carrier gas. If the thermal conductivity of the target gas is higher than that of the carrier gas, a negative voltage response occurs; conversely, a positive voltage change is observed. Hydrogen, due to its significantly higher thermal conductivity compared to the carrier gas, produces the largest negative response (28.7 mV) compared to various other gases, highlighting the device's high sensitivity to hydrogen. To better compare the performance of our thermal conductivity hydrogen sensor with other sensors, we converted the sensitivity of the developed device to normalized sensitivity, achieving a normalized sensitivity of up to 1.004×10^{-2} $\%^{-1}$. This value is superior to those of current thermal conductivity hydrogen sensors reported in the literature (Table S1), indicating significant advantages in sensitivity and detection limits for this device [18, 29–32].

3.3 Gas mixture measurement based on the H-TCS

To evaluate the hydrogen detection capability of the thermal conductivity gas sensor in complex gas atmospheres and to expand its application scenarios, we conducted a study on hydrogen testing in a four-component mixed gas environment. During the research, nitrogen, with a thermal conductivity similar to that of dry air, was selected as the carrier gas. Methane (CH_4) and carbon dioxide (CO_2) were chosen as the other two mixed interfering gases, primarily considering their thermal conductivity characteristics and their interference in practical hydrogen energy applications. On one hand, the thermal conductivity of CH_4 ($\sim$66.3 $\text{mW}\cdot\text{m}^{-1}\cdot\text{K}^{-1}$) is higher than that of N_2 ($\sim$37.9 $\text{mW}\cdot\text{m}^{-1}\cdot\text{K}^{-1}$), with a difference of 74.9%, indicating a positive difference; on the other hand, CO_2 ($\sim$32.0 $\text{mW}\cdot\text{m}^{-1}\cdot\text{K}^{-1}$) is approximately 15.6% lower than N_2, representing a weak negative difference. The combination of these gases with H_2 ($\sim$266.4 $\text{mW}\cdot\text{m}^{-1}\cdot\text{K}^{-1}$) allows for coverage of the "high-medium-low" thermal conductivity range. Furthermore, CH_4, being a major component of industrial and residential fuels, and CO_2, as an inherent component of the atmosphere and a primary component of industrial waste gases, are commonly found in hydrogen applications such as hydrogen storage and fuel cells, making them typical interfering gases. To simplify the replication of gas distribution in practical applications, we referenced the gas component concentrations derived from the separation of oil and gas after transformer oil processing to approximate the concentration of H_2, CH_4, and CO_2 (Table S2). Therefore, the choice of these two gases as interfering factors can effectively simulate the typical interference environment encountered in actual hydrogen applications, ensuring the accuracy of the thermal conductivity gas sensor in detecting H_2 in complex gas scenarios and laying a foundation for its reliable application in distributed hydrogen monitoring.

To achieve the detection of mixed gases, we further proposed a signal decoupling strategy based on multiple sensors and constructed a four-component gas analysis testing system, as shown in Figure A10, to conduct experimental

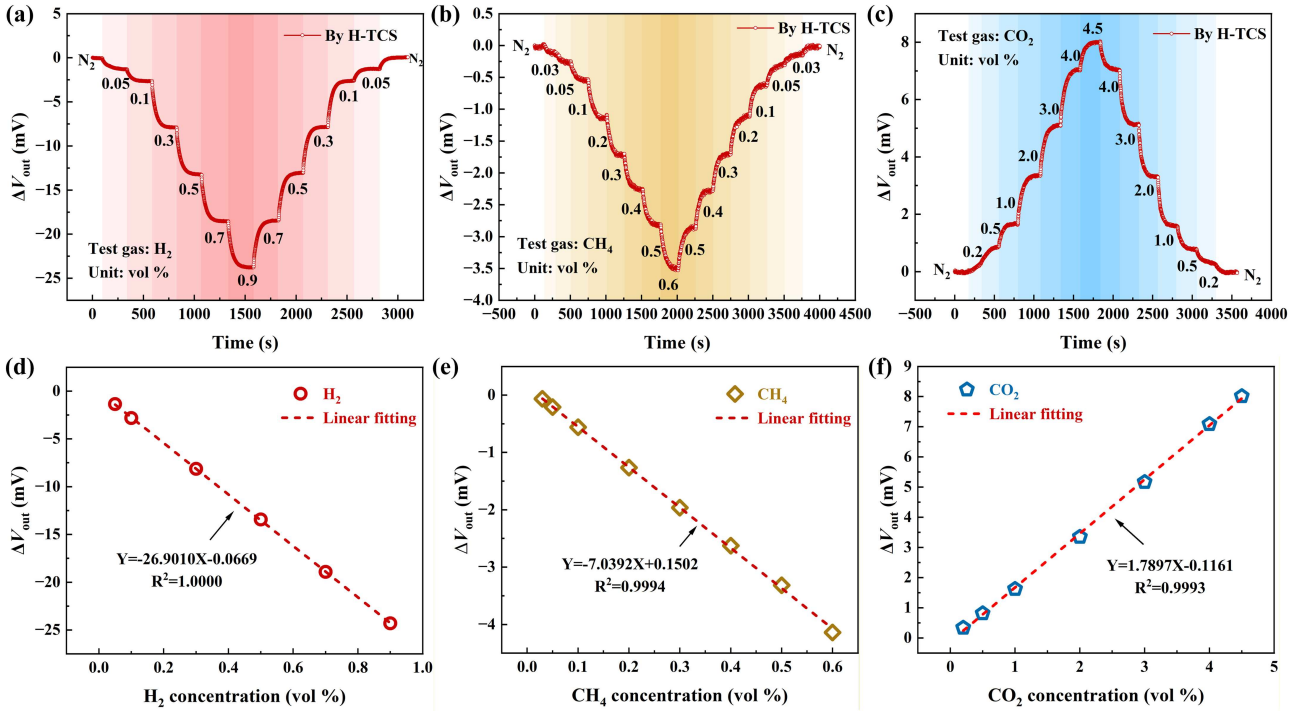

Figure 4 (Color online) Characterization of gas sensing performance of an H-TCS in gas mixtures monitoring. Voltage response curve of an H-TCS to (a) variations in H_2 concentration, (b) variations in CH_4 concentration, and (c) variations in CO_2 concentration. Voltage response curve for (d) 0.05% to 0.9% H_2, (e) 0.03% to 0.6% CH_4, and (f) 0.2% to 4.5% CO_2.

research on multi-gas measurement. In the experiments, we first utilized our self-developed non-dispersive infrared (NDIR) sensors to accurately measure the concentrations of CO_2 and CH_4 [36–38]. Subsequently, we deducted the contributions of these two gases from the response signals of the thermal conductivity gas sensor, thereby isolating the response results specifically related to hydrogen concentration, ultimately achieving accurate analysis of H_2 concentration. To accurately analyze the concentration information of various gases, we simultaneously placed the H-TCS, CO_2, and CH_4 sensors inside the gas chamber with nitrogen as the carrier gas, and tested the response of each sensor to the three target gases. The response capability of the H-TCS is shown in Figures 4(a)–(c). It can be observed that based on the physical detection principle of H-TCS, the sensor responds to all three two-component gas mixtures, but the response values exhibit significant differences due to variations in thermal conductivity. Similarly, we also obtained the relationship between the concentrations of CO_2 and CH_4 and the sensor output (Figure A11). In contrast, the CH_4 and CO_2 sensors demonstrated superior selectivity, exhibiting a stepwise concentration-dependent response to the target gases, while the voltage fluctuations caused by interference from non-target gases remained below 5 μV. Furthermore, to achieve signal decoupling, we analyzed the linear response curves and sensitivities of the H-TCS to different gases, establishing the relationship between gas concentrations and output voltages (Figures 4(d)–(f)). The analysis indicated that the sensor's responses to these three gases were all linear, with H_2 exhibiting the highest sensitivity due to the greatest difference in thermal conductivity compared to the carrier gas (N_2). Additionally, we obtained the concentration-voltage curves for the CH_4 and CO_2 sensors corresponding to CH_4 and CO_2 gases (Figure A12), facilitating the prioritized detection of interference gas concentration values.

Building on the analysis of the sensor's capability to detect two-component mixed gases, we further tested the response of three sensors to multi-component mixed gases. As shown in Figure 5(a) and Figure A13, the response of the H-TCS to the sequential introduction of CH_4, CO_2, and H_2 agreed with expectations. CH_4 (thermal conductivity slightly higher than N_2) caused a slight negative voltage shift, while CO_2 (thermal conductivity slightly lower than N_2) resulted in a positive voltage shift. In contrast, H_2 induced a pronounced negative voltage shift. Accordingly, when 0.05% CH_4 was first introduced, the output voltage of H-TCS decreased slightly. Subsequently, the introduction of 3% CO_2 raised the output voltage due to reduced thermal conductivity, followed by a stepwise voltage decrease upon the graded introduction of H_2. After sequentially stopping the flows of H_2, CO_2, and CH_4, the H-TCS output voltage returned to its baseline. These results confirm that the degree of change in output voltage is related not only to the thermal conductivity of the gases but also to their concentrations. As the gas

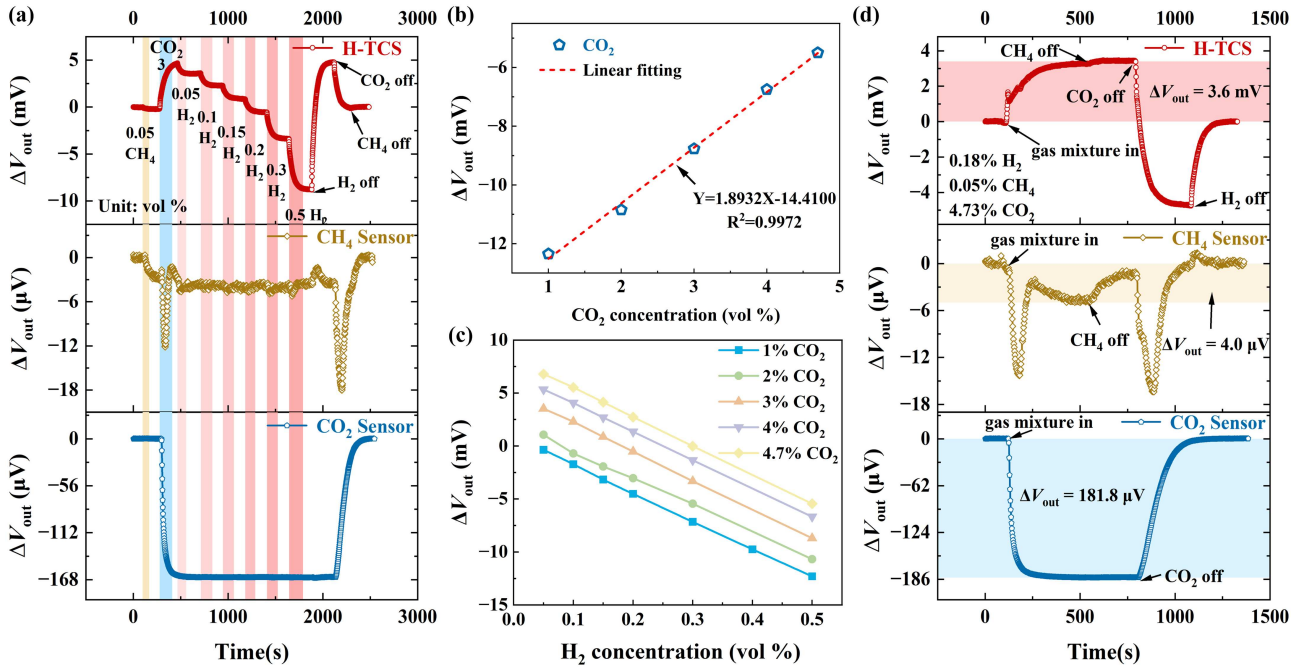

Figure 5 (Color online) Cross-decoupling signal solution analysis of multi-gas sensing systems combining an H-TCS with NDIR CO_2 and CH_4 sensors. (a) Voltage response curve of the H-TCS, CH_4 sensor and CO_2 sensor to variations in gas mixtures (0.05% CH_4, 3% CO_2, 0.05%–0.5% H_2); (b) voltage response of H-TCS to CO_2 concentration variations in gas mixtures (0.05% CH_4, 1%–4.7% CO_2, 0.5% H_2); (c) actual voltage variations corresponding to different CO_2 and H_2 concentrations in the gas mixtures (0.05% CH_4, 1%–4.7% CO_2, 0.05%–0.5% H_2); (d) voltage response curves of the H-TCS, CH_4 sensor and CO_2 sensor for a gas mixture of 0.05% CH_4, 4.73% CO_2, and 0.18% H_2.

concentrations increased, the voltage changes became more pronounced.

Additionally, we observed that the introduction and closure of CO_2 gas affected the output of the CH_4 sensor, resulting in a negative interference peak. This may be due to fluctuations in the overlapping absorption of CO_2 at the detection wavelength of CH_4 as the CO_2 concentration dynamically changed within the gas chamber. However, once the CO_2 concentration stabilized, this fixed absorption was compensated by the baseline or could be ignored due to weak absorption, allowing the output to revert to a level determined solely by the CH_4 concentration. Therefore, we can still utilize the CH_4 sensor for measuring CH_4 gas concentrations. To verify whether the presence of other gases in the mixed gas affects the H-TCS's results for single-component gases, we changed the CO_2 concentration (1%–4.7%) while maintaining fixed concentrations of CH_4 (0.05%) and H_2 (0.5%). The resulting output voltage variation curve of H-TCS is shown in Figure 5(b). Additionally, we analyzed the output voltage changes corresponding to different CO_2 and H_2 concentration values (Figure 5(c)). Using the voltage value corresponding to the carrier gas only as a zero baseline, the response of H-TCS linearly decreased with increasing hydrogen concentration while also showing a trend of equal increment with increasing CO_2 concentration. At this point, the H_2 detection curves under different CO_2 concentration backgrounds are highly consistent, further confirming the sensor's applicability in complex environments.

To validate the ability of H-TCS to detect hydrogen concentrations in complex gas environments when used in conjunction with other sensors, we performed decoupling calculations on the output signals of various sensors. In a dynamic gas mixing system, using nitrogen as the carrier gas and referencing the gas component parameters obtained from actual oil-gas separation in power systems, we adjusted the testing system for a tenfold amplification and introduced a proportionate mixed gas of CH_4, CO_2, and H_2 (0.05% CH_4, 4.73% CO_2, and 0.18% H_2). The voltage response curve of H-TCS during this process is shown in Figure 5(d). Combining the previously obtained response curves of the sensors to CH_4, CO_2, and H_2 (Figures 4(d)–(f) and Figure A12), we calculated the concentration information of the four-component mixed gases, as illustrated in Figure A14. During the calculation, we derived the CH_4 gas concentration to be 0.05% and the CO_2 gas concentration to be 4.83% (with a 0.1% difference from the actual gas amount introduced) based on the voltage changes produced by the CH_4 and CO_2 sensors during gas variation. This concentration of CH_4 and CO_2 gases resulted in an upward voltage shift of 8.31 mV in H-TCS, while the output voltage change was 3.6 mV, indicating that the influence from hydrogen was −4.71 mV. This corresponds to a calculated hydrogen concentration of 0.17%, proving that the sensor can achieve precise detection of H_2 when faced with known gas mixtures, leveraging the signal decoupling capability of multi-sensor detection.

However, the calculated value deviated by 0.01% from the actual hydrogen concentration of 0.18%, which may be attributed to the accuracy of the fitting equations used in the calculation process, as cumulative detection errors from each sensor can lead to an overall calculation error of up to 5%. Furthermore, expansion experimental data for dissolved gas analysis (DGA) indicated that when a mixed gas composed of H_2, CH_4, C_2H_6, C_2H_4, C_2H_2, CO, and CO_2 (each component at a concentration of 1000 ppm) was introduced, the sensor detected significant voltage shifts, demonstrating its sensitive perception capability for multi-component mixed gases at different concentrations (Figure A15). Building on the signal decoupling strategy proposed earlier, future work can further integrate various types of gas sensors to construct a sensor array or detection system. By synergistically incorporating intelligent algorithms to enhance the specificity and anti-interference capability of gas recognition, precise qualitative and quantitative analysis of multi-component gases in complex gas environments can ultimately be achieved.

4 Conclusion

This work developed a hydrogen gas sensor based on a thermopile structure, and it achieved precise detection of hydrogen concentration by monitoring changes in gas thermal conductivity. The sensor utilizes an X-shaped microheater to establish a distinct temperature gradient between the hot and cold ends of the thermopile. Meanwhile, series-connected double-layer stacked N/P-type polysilicon thermocouples effectively amplify the weak temperature difference signals induced by gas concentration variations. Additionally, the suspended membrane structure enhances heat accumulation and stability at the center of the device, significantly improving the sensor's sensitivity to hydrogen detection, achieving a sensitivity of 27.06 mV/% with good repeatability and stability. The fabrication process of this device is fully compatible with CMOS technology, enabling large-scale mass production. Furthermore, by combining the decoupling calculation methods of multiple sensors, this work also realized the separation and concentration detection of hydrogen signals in four-component mixed gases. Overall, this sensor integrates miniaturization, low power consumption, wide measurement range, high sensitivity, and low detection limits, making it a highly promising candidate device for applications in distributed hydrogen monitoring.

5 Experimental section

5.1 Device fabrication

The fabrication process begins with single-side polished (100) silicon wafers (Figure A3-I). Initially, a multilayer film of $SiO_2/Si_3N_4/SiO_2$ (ONO) is deposited on the wafer using plasma-enhanced chemical vapor deposition (PECVD) technology to serve as the structural support layer (Figure A3-II). Next, a phosphorus-doped N-type polysilicon layer is deposited and patterned into thermocouple strip structures via photolithography and dry etching (Figure A3-III). A silicon oxide isolation layer is then grown for insulation, followed by the formation of a P-type polysilicon thermocouple strip through deposition, boron doping, and patterning (Figure A3-IV). After that, another SiO_2 layer is deposited, and photolithography and etching are employed to create electrical connection vias (Figure A3-V). An aluminum layer is then deposited using magnetron sputtering, and through a wet etching process, the microheaters, electrodes, and wires for connecting the thermocouples in series are simultaneously patterned (Figure A3-VI). Later, SiO_2 and Si_3N_4 layers are deposited for insulation and passivation (Figure A3-VII). Finally, a deep reactive ion etching (DRIE) process is used to create cavities on the backside of the wafer, forming the closed-membrane structure (Figure A3-VIII). This process results in the realization of the thermal conductivity gas sensor.

5.2 Experimental equipment

The gas sensing test system consists of a gas chamber, gas supply unit, gas mixing system, DC power supply, digital multimeter, and computer (Figure 3(a)). The gas source cylinder provides the required gas, and the gas testing calibration device (MF-4B, Zhongke Huanyi (Beijing) Metrology Technology Co., Ltd., China) automatically regulates the gas flow and concentration. The microheater in the sensor is powered by a DC power supply (DH1766-2, Beijing Dahua Radio Instrument Co., Ltd., China), and the output voltage signal from the sensor is collected using a high-precision digital multimeter (Fluke 8846A, Fluke Corporation, America). The voltage-temperature response and thermoelectric sensitivity tests of the thermopile are conducted using a black body radiation source (DCN1000H4LT, HGH Infrared Systems, France). During the operation of the microheater, an infrared thermal imager (MAG-F6, Shanghai Magnity Technologies Co., Ltd., China) is used to monitor the temperature distribution on the sensor's surface in real-time. Additionally, a temperature and humidity generator (HygroGen2 HG2-S, Rotronic

AG, Switzerland) is employed to precisely control the environmental temperature and humidity conditions. To test the thermal response time of the sensor, a signal generator (SDG 1022X, Siglent Technologies Co., Ltd., China) supplies a 2.5 V, 5 Hz square wave voltage applied to the microheater, and the output voltage of the thermopile is filtered through a smoothing filter circuit module before being recorded by an oscilloscope (MSOX04T, Keysight Corporation, Malaysia).

Acknowledgements This work was supported in part by National Key Research and Development Program of China (Grant No. 2024YFB32-13900), National Natural Science Foundation of China (Grant Nos. 62201567, 62474192), and Youth Innovation Promotion Association and Chinese Academy of Sciences (Grant Nos. 2022117, 2022048).

Supporting information Appendix A. The supporting information is available online at info.scichina.com and link.springer.com. The supporting materials are published as submitted, without typesetting or editing. The responsibility for scientific accuracy and content remains entirely with the authors.

References

1 Smith C, Hill A K, Torrente-Murciano L. Current and future role of haber-bosch ammonia in a carbon-free energy landscape. Energ Environ Sci, 2020, 13: 331–344
2 Nielsen M, Alberico E, Baumann W, et al. Low-temperature aqueous-phase methanol dehydrogenation to hydrogen and carbon dioxide. Nature, 2013, 495: 85–89
3 Clemen C, Ravikanti M, La Bianca N, et al. Considerations for hydrogen fueled aerospace gas turbine combustion sub-system design. In: Proceedings of the ASME Turbo Expo 2024: Turbomachinery Technical Conference and Exposition, 2024
4 Farazmand M, Saadat Z, Sameti M. Above-ground hydrogen storage: a state-of-the-art review. Int J Hydrogen Energy, 2024, 90: 1173–1205
5 Kim C, Cho S H, Cho S M, et al. Review of hydrogen infrastructure: the current status and roll-out strategy. Int J Hydrogen Energy, 2023, 48: 1701–1716
6 Suwa Y. Studies on the safe application techniques of high-pressure hydrogen gas. J Phys-Conf Ser, 2024, 2812: 012002
7 Mejia A, Brouwer J, Mac Kinnon M. Hydrogen leaks at the same rate as natural gas in typical low-pressure gas infrastructure. Int J Hydrogen Energy, 2020, 45: 8810–8826
8 Swager T M, Pioch T N, Feng H, et al. Critical sensing modalities for hydrogen: technical needs and status of the field to support a changing energy Landscape. ACS Sens, 2024, 9: 2205–2227
9 Kondalkar V V, Park J, Lee K. MEMS hydrogen gas sensor for in-situ monitoring of hydrogen gas in transformer oil. Sens Actuat B-Chem, 2021, 326: 128989
10 Yin X, Wang X, Wang L, et al. Cooperative control of air and fuel feeding for PEM fuel cell with ejector-driven recirculation. Appl Therm Eng, 2021, 199: 117590
11 Zhi Z, Gao W, Yang J, et al. Amperometric hydrogen gas sensor based on Pt/C/Nafion electrode and ionic electrolyte. Sens Actuat B-Chem, 2022, 367: 132137
12 Zhong A, Shen B, Wang T, et al. Ultrafast H_2 gas nanosensor for ppb-level H_2 gas detection based on GaN honeycomb nanonetwork. Sens Actuat B-Chem, 2021, 329: 129079
13 Çoban Ö, Tekmen S, Gür E, et al. High optical response NiO, Pd/NiO and Pd/WO_3 hydrogen sensors. Int J Hydrogen Energy, 2022, 47: 25454–25464
14 Panama G, Jo M, Shim S S, et al. Hydrogen sensor with a thick catalyst layer anchored on soda-lime glass. Int J Hydrogen Energy, 2024, 55: 875–881
15 Occelli C, Fiorido T, Perrin-Pellegrino C, et al. Sensors for anaerobic hydrogen measurement: a comparative study between a resistive PdAu based sensor and a commercial thermal conductivity sensor. Int J Hydrogen Energy, 2023, 48: 17729–17741
16 El Matbouly H, Domingue F, Palmisano V, et al. Assessment of commercial micro-machined hydrogen sensors performance metrics for safety sensing applications. Int J Hydrogen Energy, 2014, 39: 4664–4673
17 Oh D W, Kang K, Lee J H. Minimum detection concentration of hydrogen in air depending on substrate type and design of the 3ω sensor. Sensors, 2023, 23: 9009
18 Zhang Y, Xie D, Yang Y, et al. High heat transfer efficiency MEMS Thermal conductivity gas sensor for hydrogen. IEEE Sens J, 2024, 24: 29678–29686
19 Harumoto T, Fujiki H, Shi J, et al. Extremely simple structure hydrogen gas sensor based on single metallic thin-wire under sweep heating. Int J Hydrogen Energy, 2022, 47: 34291–34298
20 Ng D K T, Chen W G, Wang H H, et al. Hydrogen sensor (400 ppm-1%) based on 20% ScAlN pyroelectric detector for a sustainable society. In: Proceedings of Terahertz, RF, Millimeter, and Submillimeter-Wave Technology and Applications, 2024
21 Guan Y, Lei C, Liang T, et al. Design, preparation and characterization of a double-ended symmetric MEMS thermopile with adiabatic grooves. Infrared Phys Tech, 2022, 122: 104078
22 Xu W, Li Z, Fang Z, et al. A Sub-5mW monolithic CMOS-MEMS thermal flow sensing SoC with ± 6 m/s linear range. IEEE J Solid-St Circ, 2024, 59: 1486–1496
23 de Graaf G, Wolffenbuttel R F. Surface-micromachined thermal conductivity detectors for gas sensing. In: Proceedings of the 2012 IEEE International Instrumentation and Measurement Technology Conference Proceedings, 2012. 1861–1864

24 Febrina M, Satria E, Djamal M, et al. Development of a simple CO_2 sensor based on the thermal conductivity detection by a thermopile. Measurement, 2019, 133: 139–144

25 de Graaf G, Abarca Prouza A, Ghaderi M, et al. Micro thermal conductivity detector with flow compensation using a dual MEMS device. Sens Actuat A-Phys, 2016, 249: 186–198

26 Zheng Y, Xu H, Li Z, et al. Artificial intelligence-driven approaches in semiconductor research. Adv Mater, 2025, 37: 2504378

27 Wang C, Zhang H, Gu J, et al. MEMS-based microhotplate gas sensor and sensor array for intelligent applications: a review. MicroChem J, 2026, 220: 116555

28 Hu Z, Zhao W, Cheng H, et al. Application of PSO-CNN algorithm in semiconductor gas sensors based on temperature modulation. IEEE Sens J, 2024, 24: 32717–32728

29 Berndt D, Muggli J, Wittwer F, et al. MEMS-based thermal conductivity sensor for hydrogen gas detection in automotive applications. Sens Actuat A-Phys, 2020, 305: 111670

30 Cho W, Kim T, Shin H. Thermal conductivity detector (TCD)-type gas sensor based on a batch-fabricated 1D nanoheater for ultra-low power consumption. Sens Actuat B-Chem, 2022, 371: 132541

31 Wu Z, Zhang X, Chen L, et al. Ultra-low-power, extremely stable, highly linear-response thermal conductivity sensor based on a suspended device with single bare Pt nanowire. ACS Sens, 2024, 9: 4721–4730

32 Wang C, Jiao B, Liu X, et al. Design of thermal conductivity gas sensor with silicon cap. In: Proceedings of the 2023 IEEE 16th International Conference on Electronic Measurement & Instruments (ICEMI), 2023. 204–208

33 Maruyama S, Moriya S. Newton's law of cooling: follow up and exploration. Int J Heat Mass Tran, 2021, 164: 120544

34 Akasaka S, Terumoto K, Kanno I. Temperature dependence of accuracy of thermal conductivity hydrogen sensor. In: Proceedings of the 2024 IEEE Sensors, 2024. 1–5

35 Xiang Z, Shi M, Zhou N, et al. A highly accurate method for measuring response time of MEMS thermopiles. Micromachines, 2022, 13: 1717

36 Wu J, Shi M, Zhou N, et al. A non-dispersive infrared CO_2 sensor with a paraboloid chamber and a nanoforest-enhanced thermopile detector. ECS J Solid State Sc, 2025, 14: 047005

37 Zhang Q, Li H, Han B, et al. Development of MEMS thermal emitters applicable in NDIR gas sensors: a review. IEEE Sens J, 2025, 25: 16562–16574

38 Zhang Q, Chen S, Shi M, et al. An ultra-low-power and high-temperature-homogeneity wafer-scale infrared source. Energy Environ Mater, 2026, 8: e70208